Construction and Performance of the Lead-Scintillating Fiber Calorimeter Prototypes for the KLOE Detector

A. Antonelli[b], M. Antonelli[b], G. Barbiellini[g], M. Barone[b], S. Bertolucci[b], S. Bianco[b], C. Bini[d], C. Bloise[b], V. Bolognesi[c], F. Bossi[b], P. Campana[b], F. Cervelli[c], R. Caloi[d], M. Cordelli[b], G. De Zorzi[d], G. Di Cosimo[d], A. Di Domenico[d], O. Erriquez[a], F. L. Fabbri[b], A. Farilla[a], A. Ferrari[c], P. Franzini[d], F. Garufi[d], P. Gauzzi[d], E. Gero[b], S. Giovannella[b], R. Haydar[b], M. Incagli[c], L. Keeble[b], W. Kim[f], G. Lanfranchi[b], J. Lee-Franzini[bf], A. Martini[b], A. Martinis[g], S. Miscetti[b], F. Murtas[b], A. Parri[b], A. Passeri[e], S. Sarwar[b], F. Scuri[g], E. Spiriti[e], L. Tortora[e], X. L. Wang[b], S.Wölfle[b].

[a] *Dipartimento di Fisica dell'Università e Sezione INFN Bari,*

[b] *Laboratori Nazionali di Frascati dell'INFN, Frascati,*

[c] *Dipartimento di Fisica dell'Università e Sezione INFN Pisa,*

[d] *Dipartimento di Fisica dell'Università e Sezione INFN Roma I,*

[e] *Istituto Superiore di Sanità and Sezione INFN, ISS, Roma,*

[f] *Physics Department, State University of New York at Stony Brook,*

[g] *Dipartimento di Fisica dell'Università e Sezione INFN Trieste/Udine.*

ABSTRACT

The KLOE detector is designed primarily for the study of direct CP violation in K^0 decays. The electromagnetic calorimeter, EmC, is a most demanding element of the detector. Two prototypes of the EmC (one for the *barrel* and one for the *end-cap* region) have been built at Frascati and tested at PSI (Switzerland) using beams of electrons, muons and pions of 40 to 290 MeV/c momentum, and at the Frascati LADON facility using photons of 20 to 80 MeV. We observe excellent linearity from 20 to 290 MeV. The energy resolution is $\sigma(E)/E\sim 4.4\%/\sqrt{E\ (\mathrm{GeV})}$ and the time resolution is $\sim 34\,\mathrm{ps}/\sqrt{E\ (\mathrm{GeV})}$. We found little dependence on incidence angle and entry position. We also determined that some π/μ identification is possible.

1. Introduction

The main goal of the KLOE[1] experiment at the DAΦNE ϕ–factory[2] in Frascati is to study CP violation in K^0 decays by measuring $\Re(\epsilon'/\epsilon)$ with an accuracy of $\mathcal{O}(10^{-4})$. The electromagnetic calorimeter (EmC) plays a crucial role in this measurement since $K_{L,S}$ neutral decays ($K_{L,S}\to\pi^0\pi^0$) produce four photons between 20 and 280 MeV. Identification of these decays and rejection of the $K_L\to 3\pi^0$ background[3,4] make the EmC a most demanding element of the detector. Vertex reconstruction of $K^0\to\pi^0$'s$\to\gamma$'s in KLOE can be performed by measuring the arrival time of each photon on the calorimeter surface,[3,4] because of the low speed of the K^0 ($\beta_K \sim 0.2$), requiring excellent timing accuracy of the EmC. In addition, the calorimeter should also provide a fast and unbiased first level trigger for the detector. Finally, it should have some particle identification capability, to aid rejection of $K_{\mu 3}$ decays.

We have chosen to use a lead–scintillator sampling calorimeter, consisting of very thin (0.5 mm) lead layers, in which are embedded 1 mm diameter scintillating fibers. Lead layers and fibers are mostly perpendicular to the incident particles. Calorimeters with a similar structure have already been built,[5] showing an energy resolution of $\sim 6\%/\sqrt{E\ (\mathrm{GeV})}$, though used with particles entering the calorimeter mostly along the fibers' direction. Test results for small size prototypes used in both configurations are also given in ref. 6.

For timing and position resolution considerations, fibers are the best available solution as an active medium for an $\sim$4 m long calorimeter. First, time measurements using fibers are better than those using bulk scintillators because the superior reflectivity on the core–cladding interface of fibers (as compared to bulk scintillator) allows light transmission over meters of length. Secondly, the small reflection angle reduces the spread of the light paths within the fiber, resulting in a smaller dependence of the time resolution on the particle impact position along the fiber.[7]

Simulation studies[4] lead to the following minimal requirements for the KLOE EmC:

1. Time resolution $\mathcal{O}(50\ \mathrm{ps}/\sqrt{E\ (\mathrm{GeV})})$
2. Energy resolution $\mathcal{O}(5\%/\sqrt{E\ (\mathrm{GeV})}$
3. Shower vertex resolution $\mathcal{O}(1\ \mathrm{cm})$
4. Full efficiency for γ's in the energy range 20–280 MeV
5. Hermeticity

In section 2 the structure and design of the KLOE EmC calorimeter is discussed. Section 3 describes the construction of prototypes and test beam layouts. The remaining sections present the results of test beam measurements.

2. The KLOE Electromagnetic Calorimeter

2.1 The EmC Design

The KLOE EmC has a central part, *barrel*, approximating a cylindrical shell of 4 m inner diameter, 4.3 m effective length and 23 cm thickness. The *barrel* covers the polar angle region ($49° < \theta < 131°$) and consists of 24 equal sectors, each one ~60 cm wide. Fibers run parallel to the beam. At both calorimeter ends, plexiglas light guides match the photomultipliers (PMs) to the fibers.

Two *end-caps*, 4 m in diameter and 23 cm thick, close as hermetically as possible the calorimeter. Each *end-cap* consists of 26 "C" shaped modules which run vertically along the chords of the circle inscribed in the *barrel*. At the two ends they are bent at 90°, becoming parallel to the *barrel* ends, to decrease the effects of the magnetic field on the PMs and to increase hermeticity. A quarter cross section of the KLOE calorimeter is shown in fig. 1.

Contrary to other lead–fiber calorimeters,[8] in our structure fibers run mostly transversely to the particle trajectories. This reduces sampling fluctuations due to channeling, *i.e.* showers developing along the fibers' direction, an effect particularly important at the low energies of interest.

2.2 The EmC Structure

Each module of the KLOE EmC is built by glueing 1 mm diameter blue scintillating fibers between thin grooved lead plates, obtained by plastic deformation of ~0.5 mm thick lead foils, as shown in fig. 2. Fibers are glued to the foils with optical epoxy and run parallel to each other. When layers are superimposed, fibers are located at the corners of adjacent quasi-equilateral triangles. This distribution of fibers in lead is more uniform than the one obtained stacking lead–plates and fiber–ribbons.[9] The grooves are just big enough to insure that the lead does not apply direct pressure on the fibers. Note that in our structure light travelling in the cladding is effectively removed because of the glue surrounding the fibers.

The selected fiber pitch of 1.35 mm results in a structure which has a fiber:lead:glue volume ratio of 48:42:10 and a sampling fraction of ~15% for a minimum ionizing particle. The final composite has a density of $\sim$5 g/cm^3 and a radiation length X_0 of $\sim$1.6 cm, has gained considerable stiffness and can be easily machined. The very small lead foil thickness ($< 0.1\,X_0$) results in a quasi–homogeneous structure and in high efficiency for low energy photons.

2.3 Fiber Characteristics

The fiber choice is driven by the need of matching a minimal set of specification requirements: high light yield, short scintillation decay constant and long attenuation length, while guaranteeing low costs and uniform quality for the large quantity required. Measurements of a wide variety of commercially available fibers have been carried out during the last two years, in close interaction with the producers. To determine the performance of a large number of fibers and to take into account the role of glue in suppressing the light component travelling in the cladding, we have measured samples of around 200 fibers each, 4.5 m long and structured as a basic calorimeter element of 3.5$\times$3.5 cm^2. Six different kinds of fibers have been measured at the T10 test beam area of PS at CERN; a detailed report on this subject can be found elsewhere.[10,11] The measurements indicate that the following fibers emitting in the blue-green region: Kuraray SCSF-81, Bicron BCF-12 and Pol.Hi.Tech-46, satisfy our specification requirements. They yield 60–90 photoelectrons (pe) with a bialkaline photocathode PM, per minimum ionizing particle crossing the 3.5$\times$3.5 cm^2 block described above, at a distance of 20 cm from the PM. Their decay constant is $\sim$2.5 ns and the attenuation lengths are between 2.7 and 3.3 m.

2.4 The Light Collection System

Since the timing resolution depends on the calorimeter light yield, great care has been put in maximizing the efficiency of the light collection system. Of equal importance is to guarantee uniform photocathode illumination, to average out its response variation.

Each light guide consists of a tapered mixing part, where the quadrangular entrance face passes smoothly to its inscribed circle, and a Winston cone concentrator.[12,13] The latter part matches the area of the calorimeter element to the sensitive photocathode face, with an area reduction factor of up to 3. This is possible, without losses[14] from Liouville's theorem, because of the small divergence angle, 22°, of the light travelling in the fibers. Measurements on the prototype's light guides give a collection efficiency of $\sim$90% with an area reduction factor of 2.7, most of the losses are consistent with being due to the additional interfaces.

3. Experimental Setup

3.1 Prototypes Assembly

We built a *barrel* prototype module of dimensions $14\times24\times203$ cm^3 to establish construction procedures and perform realistic tests of the final EmC performance, see fig. 3a). The module depth of 24 cm is equivalent to a thickness of 15 X_0. The calorimeter consists of 207 lead and scintillating fiber layers for a grand total of 21,450 fibers[15] and a weight of 330 kg.

The prototype was assembled in the Frascati machine shop. The grooved lead foils were produced with a home-made rolling machine starting from 0.5 mm thick lead foils. The grooved rollers, made of hardened steel and ground to shape by a sintered diamond tool, are mounted with ball bearings on a very rigid frame and are aligned and checked with a set of micrometers. Foils of almost 6 m length, 15 cm wide have been produced. The thickness uniformity obtained is around few tens of μm, the grooves deviate from a straight line by less than 0.1 mm per meter of foil length.

The prototype was constructed by glueing the first lead foil to a 2 cm thick iron back plate carrying all the mounting fixtures. Epoxy[16] was then applied in a precisely measured amount to the top surface of each lead foil. A layer of fibers was then laid down in the grooves and epoxy applied anew. Typically, 6–7 layers of fibers and lead were stacked in about one hour, before the glue started curing. The growing stack was then compressed under vacuum for at least 30 min to apply uniform pressure, and to squeeze out excess glue. Once the final thickness was reached the two ends were cut and milled. No fiber was damaged during the stacking phase, while four fibers were lost during the final milling. The calorimeter was wrapped in a 1 mm thick steel skin, in order to simulate the final design and provide protection for the module.

A prototype for the *end-cap* region, fig. 3b), consisting of two "C" shaped modules, was also built. The width of each module is 7 cm and they both have the same depth of 24 cm. Each section consists of a central straight piece (89–110 cm), two curved pieces with an inner radius of 7.5 cm, and two straight end pieces to which light guides are glued.[15] It has been constructed by cutting the grooved lead foils and fibers to the desired lengths, incising at the two ends the central groove of each lead foil, leaving the central part uncut for a length of 89 cm, then bending the two adjacent modules.

The readout, identical for both prototypes, was organized into 22 elements for each side: five planes of four small elements, 3.5×3.5 cm^2, and two large rear elements, 6.5×7

cm^2, see fig. 3b). For the small elements, on each side the light was transported from the calorimeter through light guides to 1-1/8 inch diameter PMs, with an area concentration factor of $\sim$2.7. For the beam tests, commercially available PMs with a good transit time spread ($<$ 1 ns) have been used.[17] The rear elements were similarly coupled to 5 cm diameter PMs, with an area concentration factor of $\sim$2.5.

In order to investigate the effect of coarsening the readout granularity and using larger light guides, we took data with the *barrel* readout organized in four planes of three 4.2×4.2 cm^2 cells, leaving the last plane unchanged. This configuration is referred to as "coarse" granularity, see fig. 3a). Since the same PMs were used, the light guides had an area concentration factor of $\sim$3.8.

3.2 Test Beams Layout

The calorimeter prototypes have been tested[18–21] in a beam at the Paul Scherrer Institut, PSI, in Villigen, Switzerland. The PSI machine is an isochronous cyclotron which accelerates protons to 600 MeV kinetic energy. A secondary beam of π's, μ's and e's in the momentum range 50–400 MeV/c was delivered to the test areas.

Two crossed scintillators in front of the calorimeter and a third counter, 4.5 m away from the calorimeter, fig. 4, provided a beam trigger, defined the beam position at the calorimeter and enabled $\pi/\mu/e$ identification by time of flight.

The calorimeter PM outputs were connected to active splitters through 5 m of RG-58 cable. The two outputs of each splitter were sent to CAMAC ADCs, to low threshold (5 mV) discriminators, the signal for 50 MeV being $\sim$350 mV. The discriminator outputs acted as TDC stops. The trigger signal was used to generate the ADC gates and the reference time signal T_0 which supplied the "start" for the TDC system.

The *barrel* prototype has also been tested with tagged low energy photons (20–80 MeV) at the Frascati LADON facility.[22] The LADON photons were obtained by back scattering a laser beam by the electrons stored in ADONE. A tagging system for the scattered electrons yields a determination of the photon energy with a resolution of $\sim$1.7 MeV. The trigger was obtained by a coincidence from the two calorimeter ends, after adding all signals from each side. The trigger generated ADC gates and TDC "start"s which were cleared if there was no trigger from the tagging system within 200 ns.

4. Energy Response and Resolution

The coordinate system used in the data analysis is shown in fig. 4, where the definition of the incidence angle θ is also indicated. The origin was put in the center of the calorimeter surface facing the beam.

In order to study the energy response of the prototype we define the total visible energy E_{vis} as the sum over all elements read out on both ends, labelled A and B. To correct for the response of each channel we divided the signal $E_{adc,i}$ of channel i, by the calibration constants $K_{mip,i}$:

$$E_{vis} = \sum_{i=1}^{N} \frac{1}{2} (E_{A,i} + E_{B,i}) \text{ with } E_i = \frac{E_{adc,i}}{K_{mip,i}} \; . \tag{1}$$

The calibration constants K_{mip}, in ADC counts, were obtained with cosmic rays and 400 MeV/c pions incident at the center of each element. Clean samples of events selected for the calibration were ensured by means of triggering and software cuts. A gaussian fit to the pulse height distribution was performed for each channel to determine the peak position. The fit interval was chosen to be asymmetric with respect to the mean value, to take into account the asymmetric shape of the distribution.

We define 1 MIP as the visible energy deposited by a minimum ionizing particle in a 3.5×3.5 cm^2 readout element; our simulation[23] determines 1 MIP to be equivalent to an average energy deposit of 3.24 MeV in the active material. For the coarse granularity and for the larger cells of the last plane geometrical correction factors have been used to express the results in our calibration units. Pions of 400 MeV/c momentum are minimum ionizing particles to a reasonable approximation only in the first plane of the calorimeter. We have therefore corrected for the increase of the specific ionization with calorimeter depth and for straggling effects. The correction factors used for both granularities are given in table 1.

Before reaching the calorimeter the beam had to pass through the trigger counters and the iron skin of the calorimeter itself. The total amount of material is equivalent to 3.6 cm of scintillator. Positrons therefore lose around 7 MeV while the energy loss of pions and muons depends on their kinetic energy and was appropriately taken into account. These corrections have been applied to the beam energy of the charged particles.

4.1 Energy Response and Resolution for Photons and Positrons at the Calorimeter Center

The following results were obtained with positrons and photons entering the center of the calorimeter front face ($z = 0$ cm, $\theta = 0°$). The distributions of the visible energy for photons ranging from 28 to 63 MeV are displayed in fig. 5. Their shapes are well described by gaussian distributions. For each spectrum a gaussian fit with all three parameters free has been performed; the mean of the fit was used as the average calorimeter response E_{vis} and the square root of the variance $\sigma_{E,vis}$ was used to compute the energy resolution.

The plot of E_{vis}/E *vs.* the energy E of fig. 6 shows a maximum deviation from linearity of less than 3%, it is due probably to improper beam settings.

The line shapes for positrons in the energy range 40–240 MeV are shown in fig. 7 for *barrel* data with the coarse granularity. The linearity of the response is excellent, with a deviation of at most 2% as shown in fig. 8. Fitting photon and positron data together we obtain a slope $s_{barr} = (36.8 \pm 0.2)$ MIP/GeV, see fig. 9. In the same plot we have also added data for the *end-cap* prototype exposed to positrons (triangle symbols) for which the slope is $s_{ecap} = (37.4 \pm 0.6)$ MIP/GeV.

The average response to electromagnetic (e.m.) showers is proportional to the incident particle kinetic energy only if the shower is fully contained. Simulations[23] show that the depth of the prototype keeps leakage below the 2% level for the energy range of interest. The sampling fraction for e.m. showers can therefore be estimated as

$$f_{em} = E_{vis}/E = (36.8 \pm 0.2) \text{ MIP/GeV} \times 3.24 \text{ MeV/MIP} = (11.9 \pm 0.1)\%. \qquad (2)$$

The fluctuation of the ratio R between the energy signals, from each readout element, E_A and E_B at the two calorimeter ends, $R = E_A/E_B$, allows us to estimate the number of photoelectrons N_{pe}/PM. Under the assumption that quantum efficiencies and optical couplings are the same for both ends, and neglecting any correlation between E_A and E_B, we obtain $N_{pe} = (\sqrt{2} \times \mu_R/\sigma_R)^2$, μ_R and σ_R are the mean of R and the r.m.s. spread of its distribution respectively. For the *barrel* prototype the typical signal for a minimum ionizing particle at 1 m distance from the photomultiplier is $\sim$65 pe. Results within 10% were obtained by measuring the PM gain directly. The total calorimeter response is therefore around 5000 pe/GeV. A lower light yield of $\sim$50 pe/MIP is obtained in the *end-cap* prototype due to the worse quality fiber used in its construction.

The energy resolution found for positrons is

$$\frac{\sigma_{E,vis}}{E_{vis}} = \frac{(4.47 \pm 0.02)\%}{\sqrt{E \text{ (GeV)}}} \qquad (3)$$

and for photons is

$$\frac{\sigma_{E,vis}}{E_{vis}} = \frac{(4.35 \pm 0.01)\%}{\sqrt{E \text{ (GeV)}}}. \qquad (4)$$

Both e^+ and γ data are plotted together in fig. 10. The $1/\sqrt{E}$ dependence indicates that sampling fluctuations and photoelectron statistics determine the resolution. The contribution of the latter has been evaluated from the light yield to be $1.6\%/\sqrt{E}$ and is therefore negligible. A similar analysis for the *end-cap* gives an energy resolution of

$$\frac{\sigma_{E,vis}}{E_{vis}} = \frac{(4.59 \pm 0.04)\%}{\sqrt{E\ (\mathrm{GeV})}}. \tag{5}$$

The *end-cap* data are also shown in fig. 10.

4.2 Energy Response and Resolution for Pions and Muons

The response for muons and pions in the momentum range 150–280 MeV/c, of interest for the KLOE experiment, has also been studied. Due to their low kinetic energy (50–180 MeV) these particles lose energy mostly by ionization and could stop in the calorimeter. A typical energy spectrum for muons of 107 MeV is shown in fig. 11a). The small tail, at high energies, is due to muon decays while the ADC integration gate of 200 ns is open. Contributions from pion–nucleus interactions can be observed as tails in the pion spectrum, both at low and high energies. The main contribution to the signal is still due to ionization as shown in fig. 11b). The determination of the peak was therefore performed by fitting a gaussian in a narrow region around the mean.

The response *vs.* kinetic energy for both types of particles is shown in fig. 12. Points for non–zero incident angle have been included, since particles with energies higher than 140 MeV do not range out in the calorimeter. The response for muons and pions is identical. A linear fit gives a slope s_μ=46.8 MIP/GeV, corresponding to a sampling fraction for muons of

$$f_\mu = E_{vis}/E = 46.8 \pm 0.4\ \mathrm{MIP/GeV} \times 3.24\ \mathrm{MeV/MIP} = 15.2 \pm 0.1\% \tag{6}$$

and an "e/μ" ratio of f_e/f_μ=0.79. The energy resolution, shown in fig. 13, does not scale perfectly with $1/\sqrt{E}$ because sampling fluctuations become larger near the end of the particle's range. However, an approximate parametrization of the resolution is given by $3.7\,\%/\sqrt{E}$.

4.3 Dependence on the y–coordinate

To study the energy response and resolution of the calorimeter in the region between two readout elements, a precise scan in the vertical direction was performed with photons. Data were collected in the energy range 45–55 MeV with the photons hitting the calorimeter at nine different y–positions from -20 to $+20$ mm with respect to the central boundary. The beam spot size was smaller than 1 mm.

The dependence of the energy signal *vs.* the beam position y_{nom} is shown in fig. 14. The response curve shows a loss of about 10% at the center of the scan; the fall at higher and lower y–values is due to lateral leakage. The energy resolution deteriorates by 10% from $4.4\%/\sqrt{E}$ to $4.8\%/\sqrt{E}$.

4.4 Dependence on the z–coordinate

A z–scan along the module axis was performed with 190 MeV/c positrons at seven different z–positions from -80 to $+80$ cm. The z dependence of the signal is well represented as

$$E_{vis}(z) = E_{vis}(0)\cosh(z/\lambda) \tag{7}$$

where λ is the fiber attenuation length given by $\lambda = 240$ cm, fig. 15a), as derived from summing two exponentials. The measured energy resolution is shown in fig. 15b). No dependence on the z–position can be observed, confirming that sampling fluctuations are dominating the resolution of the calorimeter.

4.5 Dependence on the Incidence Angle

The response of the *barrel* prototype as a function of the incidence angle θ has been studied using photons, positrons and muons at 30°, 45° and 60° incidence. The calorimeter response does not depend on θ as expected for a calorimeter with a large sampling fraction and very thin converter layers. The distribution of E_{vis} *vs.* θ for 190–240 MeV/c positrons and 26–76 MeV photons is shown in fig. 16. The θ dependence of the response for muons was shown in fig. 12.

The energy resolution for positrons and photons was also found to be independent of the incidence angle, as can be seen in fig. 17, while a small worsening at $\theta = 60°$ for the photon data can be observed. Again, straggling at the end of charged particles' range results in larger sampling fluctuations at large incidence angles.

The curved parts of the *end-cap* prototype have been investigated by scanning the prototype with 190 MeV/c positrons incident at 45° at different positions, moving along the outer surface of the bent part. No appreciable variation was found in the scan.

5. Timing Performances

In the following we discuss the timing performance of the calorimeter for electrons, photons and muons entering the center of the *barrel* prototype with incidence angles of $0°$, $30°$, $45°$ and $60°$. The dependence of the time resolution on the coordinate z, along the fibers, is given in section 5.4. The time difference of the signals at the two ends allows us also to reconstruct the z-coordinate; a discussion of this can be found in section 5.5.

5.1 The Time Measurement Method

To measure the particle arrival time on the calorimeter, each PM signal after triggering a discriminator, was used as a TDC "stop". The "start" of the TDC system was given by an external trigger for charged particles or by an analog sum of the calorimeter signals for low energy photons, as discussed in sect. 3.2.

Timing accuracy is mostly limited by the light yield, the emission time distribution of the fibers, and by the transit time spread of the photomultipliers. In addition the measured time depends also on the shape and amplitude of the signals, and on the type of discriminators used. The dynamic range of pulse heights in the test beam spans more than one order of magnitude. Leading edge discriminators introduce a time walk depending on pulse height which has to be corrected off–line.

The dependence of the time measurement on the pulse height for a single calorimeter element exposed to 240 MeV e^+ is shown in fig. 18a). The time distribution for the same events is shown in fig. 18b); one can observe tails due to the time walk. To correct for this effect the data of fig. 18a) have been fitted with the function: $a + b/\sqrt{x}$. The corrected time distribution is displayed in fig. 18c). A further improvement in the time measurement is achieved by averaging more calorimeter elements, after correcting for each channel offset. The times measured at each calorimeter end T_A, T_B are obtained by the energy weighted average over all elements:

$$T_A = \frac{\sum_i E_{A,i}\, T_{A,i}}{\sum_i E_{A_i}}; \quad T_B = \frac{\sum_i E_{B,i}\, T_{B,i}}{\sum_i E_{B_i}} \ . \tag{8}$$

The average of T_A and T_B then defines the mean arrival time T; the distribution of T for 240 MeV e^+ at θ=0° is shown in fig. 18d). Each T spectrum is well described by a gaussian.

To obtain the net calorimeter resolution σ_T we have to unfold the time jitter σ_{st} of the "start" signal. The charged particles trigger is given by triple coincidence of counters S_1, S_2 and P, see fig. 4, but its timing is determined only by S_1. The signal from S_2 is also used as stop of a TDC channel allowing the measurement of the r.m.s. fluctuation, σ_{S_2}, of the relative time response of counters S_1 and S_2. Assuming identical response for the counters S_1 and S_2 we can estimate the time reference jitter as $\sigma_{st}=\sigma_{S_2}/\sqrt{2}\sim 60$ ps, which is the value used for obtaining the resolution results.

For the case of low energy photons no external precise trigger was available. We perform our analysis in terms of the time difference

$$\Delta T = \frac{1}{2}\frac{\sum_i E_i\,(T_{A,i} - T_{B,i})}{\sum_i E_i}, \tag{9}$$

ΔT and T are the difference and sum of T_A and T_B and therefore have the same r.m.s. spreads, *i.e.* $\sigma_{\Delta T}=\sigma_T$ except for the fact that the "start" time jitter is cancelled event by event in ΔT. The same analysis was also performed for positron data. Comparison of the results confirms the validity of our unfolding of σ_{st}.

5.2 Timing Resolution at Normal Incidence

The dependence of $\sigma_{\Delta T}$ on beam energy for 20–80 MeV γ's and of σ_T for 40–240 MeV positrons, at normal incidence on the calorimeter surface, are shown together in fig. 19. The parametrization $\sigma(T$ or $\Delta T)$=34 ps/$\sqrt{\mathrm{E\ (GeV)}}$ fits all the data well. Fitting all measurements of $\sigma_{\Delta T}$ from 20 to 240 MeV gives $\sigma_{\Delta T}$=36 ps/$\sqrt{E\ \mathrm{(GeV)}}$, in excellent agreement with the result requiring unfolding of the "start" uncertainty. The scaling with energy shows the expected dependence on the light yield.

The measurements of the time resolution with coarse granularity, triangle symbols in fig. 19, are consistent with the fine granularity ones, although the light guides area reduction factor increases from 2.7 to 3.8. This proves that light collection efficiency is unchanged.

For the *end-cap* prototype we find a time resolution of σ_T =40 ps/$\sqrt{\mathrm{E(GeV)}}$, with 40–190 MeV/c positrons. The slightly worse resolution compared to the *barrel* result is consistent with the lower light yield of the *end-cap* prototype.

5.3 Timing Resolution Dependence on Incidence Angle

The dependence of σ_T on θ is plotted for all available beam energies in fig. 20. At 60° the resolution for 240 MeV/c positrons is $\sim$25% worse than the result for normal incidence. The distributions are still gaussian. At lower energies the angular dependence of the resolution becomes negligible, being dominated by sampling fluctuations.

We have also studied the behaviour of the curved portion of the *end-cap* prototype for various entry positions at 45° incidence angle. For the most extreme conditions, when the shower effectively crosses the fibers twice, the time resolution deteriorates by ~20%.

5.4 Timing Resolution Dependence on z-Coordinate

All our measurements confirm that the time resolution scales as the number of photons to the $-1/2$ power. We therefore expect that the resolution is best at the center of the calorimeter. Using eq. (7), see sec. 4.4, the z dependence of the time resolution is given by:

$$\sigma_T(z) = \sigma_T(0)\sqrt{\cosh(z/\lambda)} \ . \tag{10}$$

This has been verified with the data from the z–scan. The resolution at the two ends of the *barrel* module is ~1.05 times worse than at the center.

5.5 Measurement of the z–Coordinate

The z–coordinate of the entry point z_e obtained from the time difference ΔT and the effective light propagation speed in the fibers v_f is:

$$z_e = v_f \Delta T \ . \tag{11}$$

ΔT is plotted *vs.* the nominal z–position in fig. 21. From a fit to the data we obtain v_f=17.2 cm/ns, in agreement with the refractive index of the fiber core, n=1.6, and the bounce angle in the fiber.

The position resolution σ_z, given by $\sigma_z = v_f \sigma_{\Delta T}$ therefore is σ_z=6 mm/$\sqrt{E \text{ (GeV)}}$ for the e.m. showers.

6. Particle Identification

The $K_L \to \pi\mu\nu$ decay, $K_{\mu 3}$, constitutes the most significant background to the identification of $K_L \to \pi^+\pi^-$ decays. The calorimeter can provide some π/μ identification to improve the background rejection from kinematics.[24] This π/μ identification can be obtained by time of flight and by energy deposition patterns.

6.1 $K_{\mu 3}$ Rejection using Time of Flight

By combining the calorimeter timing information with measurements in the KLOE central drift chamber, we can construct a χ^2 function assuming specific particle masses.

Specifically:

$$\chi^2_{ToF} = \frac{(\Delta T_s - \Delta T_p)^2}{\sigma^2} \, , \tag{12}$$

where ΔT_s is the observed difference between the arrival times of the two particles and ΔT_p is the value computed from the measured momenta, assuming that both particles are pions.

Appropriate cuts in this function can result in $K_{\mu 3}$ rejection factors of 5–6, with 93% signal efficiency, as obtained by a Monte Carlo study.[4]

6.2 $K_{\mu 3}$ Rejection using Energy Deposition Pattern

The energy deposit pattern method has been tested with data collected during the calorimeter tests for pions and muons of 200–250 MeV/c. It is based on the use of the energy signals and the first and second moments of the energy deposition distributions. Specifically the variables used are the energy released in each plane E_{plane}, the energy weighted average $\overline{X}$, and its rms spread, *i.e.* the square root of the variance, δX, defined as:

$$\overline{X} = \frac{\sum_i X_i E_i}{\sum_i E_i} \tag{13}$$

$$\delta X = \sqrt{\frac{\sum_i (X_i - \overline{X})^2 E_i}{\sum_i E_i}} \tag{14}$$

where X_i and E_i are the x–coordinate and energy release in the i^{th} calorimeter cell. Distributions of $\overline{X}$ for 200 and 250 MeV/c muons and pions θ=0° are shown in fig. 22a) and b), for the fine readout segmentation. Fig. 22c) and d) show the same distribution for the coarse readout.

With appropriate cuts on these variables, a rejection factor of 5 for muons is easily obtained, maintaining an efficiency of 95% for pions.

7. Conclusions

We studied extensively the performance of both the *barrel* and *end-cap* prototypes of the KLOE calorimeter. The energy and time resolutions are respectively σ_E/E=4.4%/$\sqrt{E\ (\mathrm{GeV})}$ and σ_T=34 ps/$\sqrt{E\ (\mathrm{GeV})}$. The former is independent of incidence angle and the latter is degraded by a factor of ~1.25 at 60°. We have also verified that a ~25% coarser readout segmentation does not affect the calorimeter performance.

Extrapolating the results described to a 4.5 m long barrel module of the final calorimeter we expect:

$$\sigma_E/E \sim 4.5\%/\sqrt{E\ (\mathrm{GeV})}$$

$$\sigma_T \sim 46\mathrm{ps}/\sqrt{E\ (\mathrm{GeV})}\ ,$$

which satisfy, with some safety margins the requirements of the KLOE experiment.

The calorimeter also provides some means to identify pions and muons.

ACKNOWLEDGEMENTS

We thank the PSI management and technical staff for their hospitality, help and support during our work at PSI. We acknowledge the efforts of the SPECAS mechanical shop: G. Cattiti, A. De Paolis, A. Di Virgilio, G. Ferretti, E. Iacuessa, L. Iannotti, U. Martini, A. Mecozzi, A. Oliveri, A. Tiburzi, and S. Valeri, led by G. Bisogni for the construction of the prototypes. We also thank A. Balla and G. Corradi for help with the electronics, D. Fabbri, L. Passamonti and V. Russo for the help at PSI, and especially M. Anelli and A. Rutili for their help in setting up and testing the calorimeter. We are indebted to W. Kluge and his group for their help during the test run. Finally, we wish to thank the LADON group for their help and collaboration.

REFERENCES

1. The KLOE Collaboration, *A GENERAL PURPOSE DETECTOR for DAΦNE*, LNF-92/019 (1992).
2. G. Vignola, *Proc. of the XXVI Int. Conf. on High Energy Physics*, ed. J. Sanford AIP (1992) 1941.
3. C. Bloise, *Proc. Workshop for Detectors and Physics at DAΦNE* , INFN-LNF (1991) 495.
4. The KLOE Collaboration, *THE KLOE DETECTOR, Technical Proposal*, LNF-93/002 (1993).
5. D. W. Hertzog *et al.*, Nucl. Instr. and Meth. A 294 (1990) 446.
6. D. Babusci *et al.*, Nucl. Instr. and Meth. A 332 (1993) 444.
7. M. Kuhlen *et al.*, Nucl. Instr. and Meth. A 301 (1991) 223.
8. D. Acosta *et al.*, Nucl. Instr. and Meth. A 294 (1990) 193.
9. P. Sonderegger, Nucl. Instr. and Meth. A 257 (1987) 523.
10. G. Barbiellini *et al.*, KLOE note 72 (1993), unpublished.
11. G. de Zorzi, *Proc. of 4th International Conference on Calorimetry in High Energy Physics*, La Biodola, Italy (1993).
12. H. Hinterberger, R. Winston, Rev. Sci. Instr. 37 (1966) 1094.
13. W. T. Welford, R. Winston, *The optics of non–imaging concentrators*, Academic Press, New York (1978).
14. R. Garwin, Rev. Sci. Instr. 23 (1952) 755.
15. For the *barrel* we used Kuraray SCSF-81 fibers in the first 3.5 cm of the calorimeter and SCSF-38 fibers elsewhere. For the *end-cap* we used Kuraray SCSF-81 fibers for the innermost 7 cm and Pol.Hi.Tech-46 elsewhere.
16. Bicron optical epoxy resin BC 600 ml.
17. 1-1/8′ Hamamatsu phototubes, type R1398.
18. F. Murtas, presented at the 5th Topical seminar on experimental apparatus for high-energy particle physics and astrophysics, San Miniato, Italy (1993)
19. F. Bossi, *Proc. of Int. Europhysics Conf. on High Energy Physics EPS'93*, eds. J. Carr and M. Perrottet, *Editions Frontiere* (1993) 393.
20. S. Miscetti, *Proc. of 4th International Conference on Calorimetry in High Energy Physics*, La Biodola, Italy (1993).

21. S. Sarwar, *Workshop on Scintillating Fiber Detectors*, Notre Dame, USA (1993).

22. D. Babusci *et al.*, Nucl. Instr. and Meth. 305 (1991) 19.

23. S. Miscetti and A. Parri, KLOE note 111 (1994), unpublished.

24. The KLOE Collaboration, *The KLOE Central Drift Chamber*, LNF-94/028 (1994).

Table 1. Specific ionization correction factors.

Plane Number	1	2	3	4	5	6
3.5×3.5	1.00	1.03	1.04	1.06	1.10	1.14
4.2×4.2	1.01	1.04	1.05	1.09	1.14	–

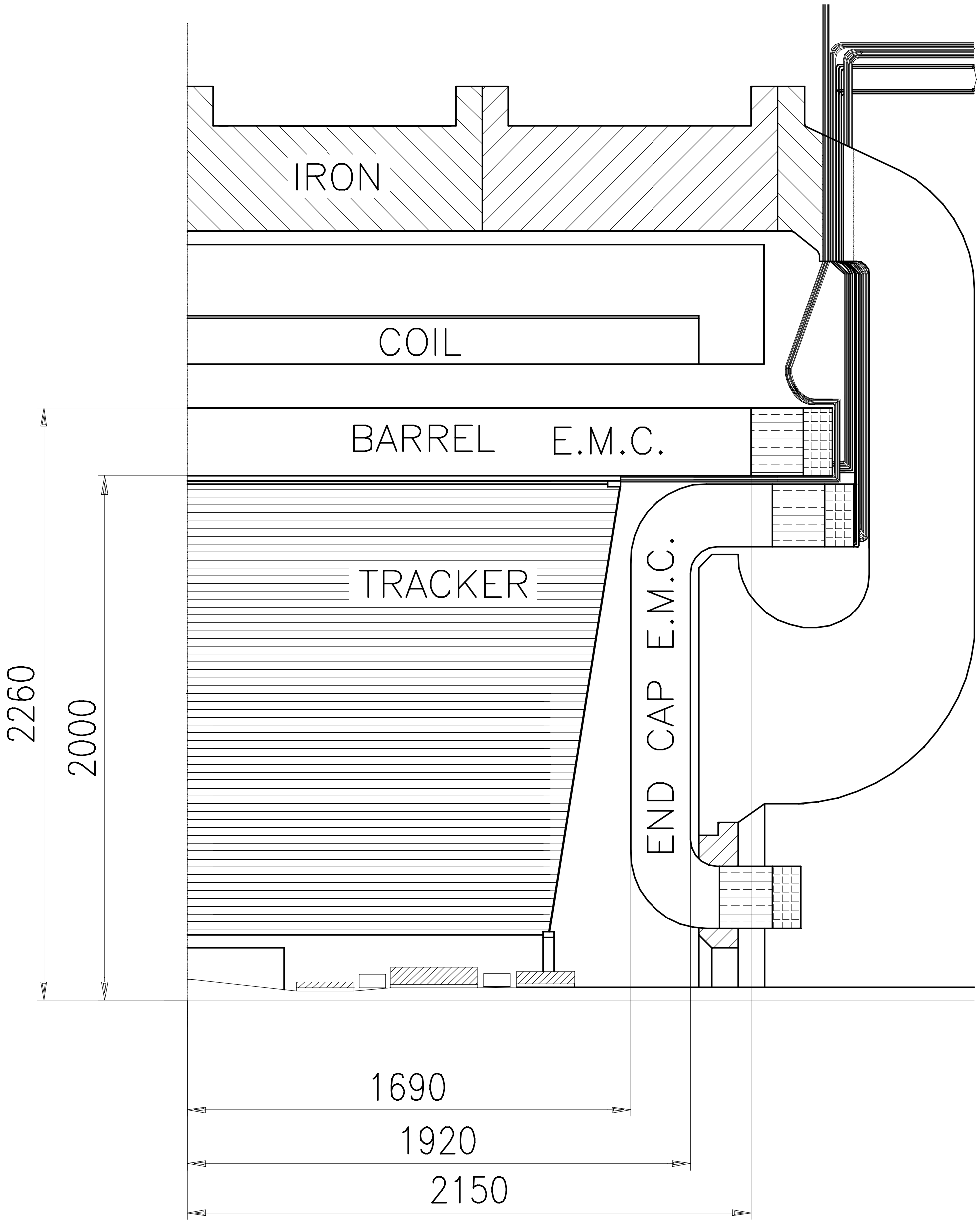

Fig. 1. Cross section of the KLOE calorimeter.

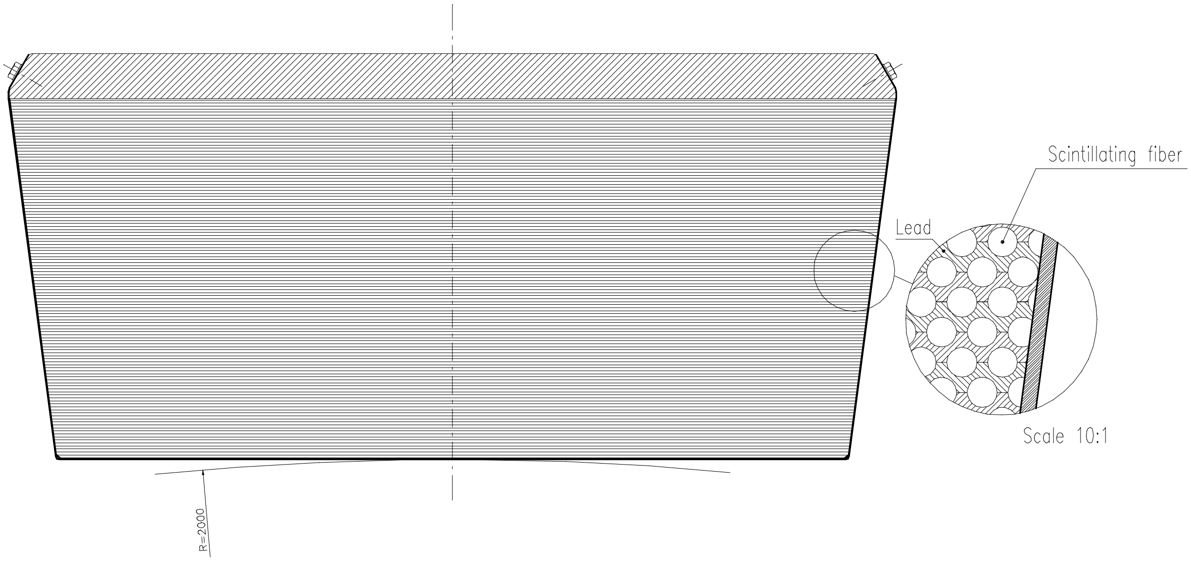

Fig. 2. Fiber and lead layout.

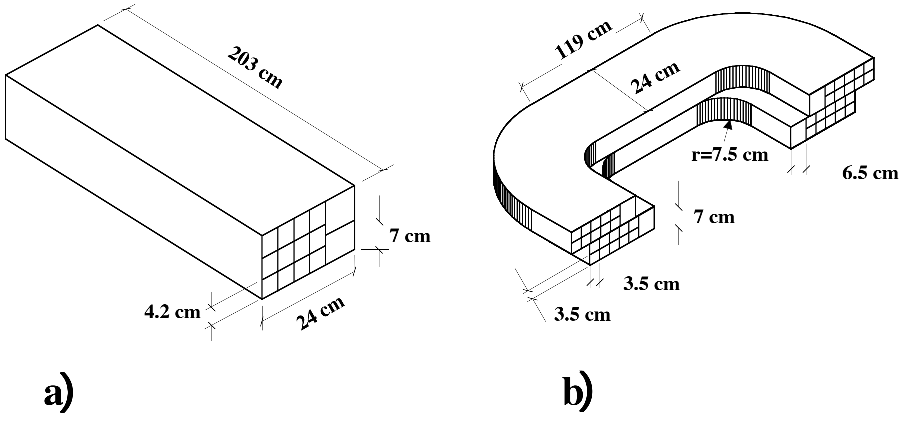

Fig. 3. a) *Barrel* and b) *end-cap* prototype.

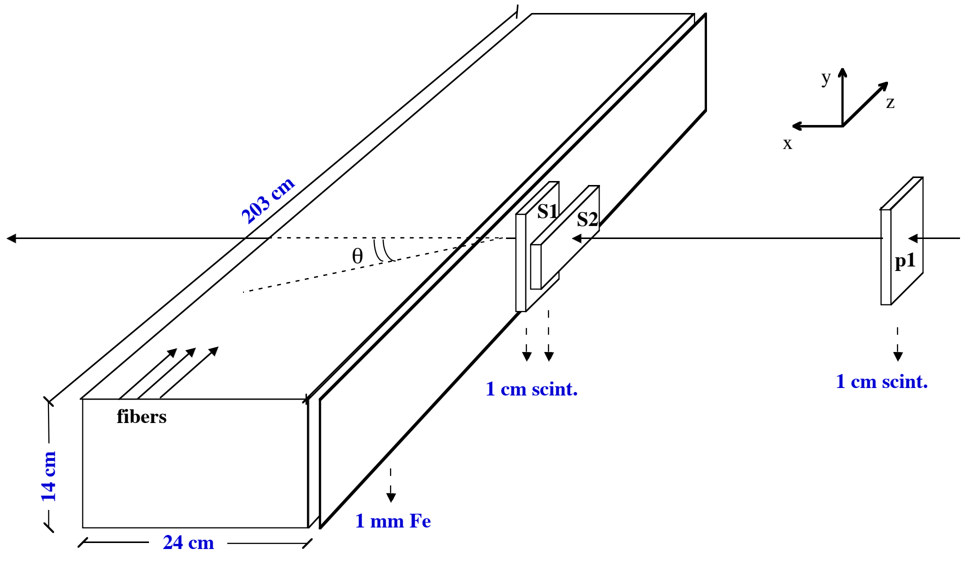

Fig. 4. Layout of the test beam at PSI.

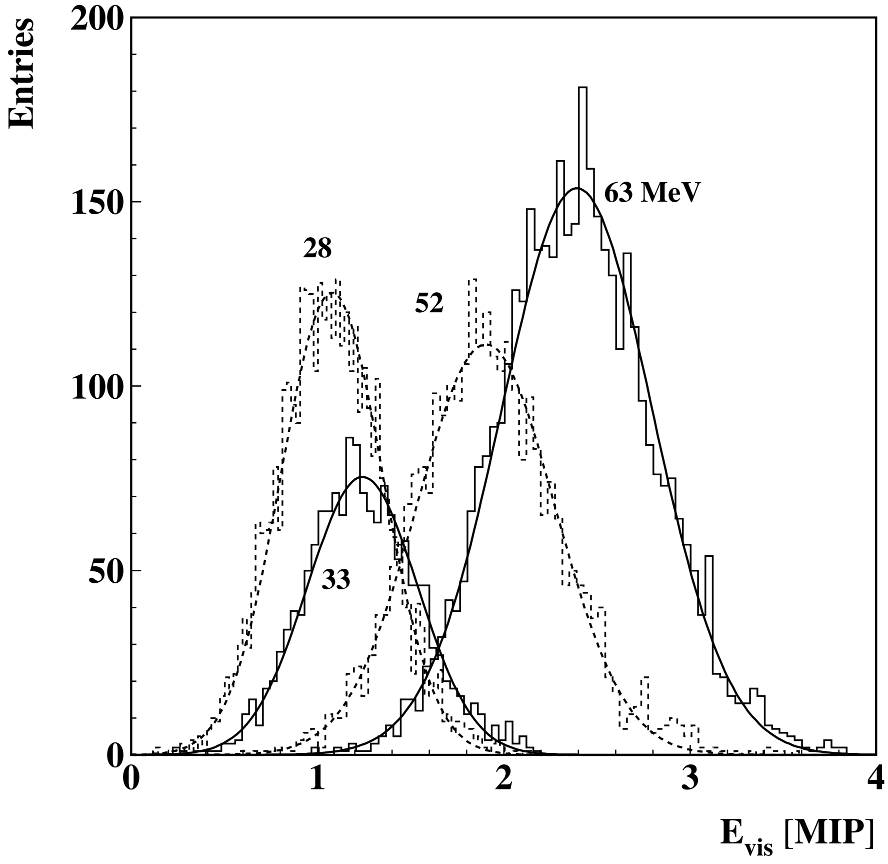

Fig. 5. Energy spectra for photons.

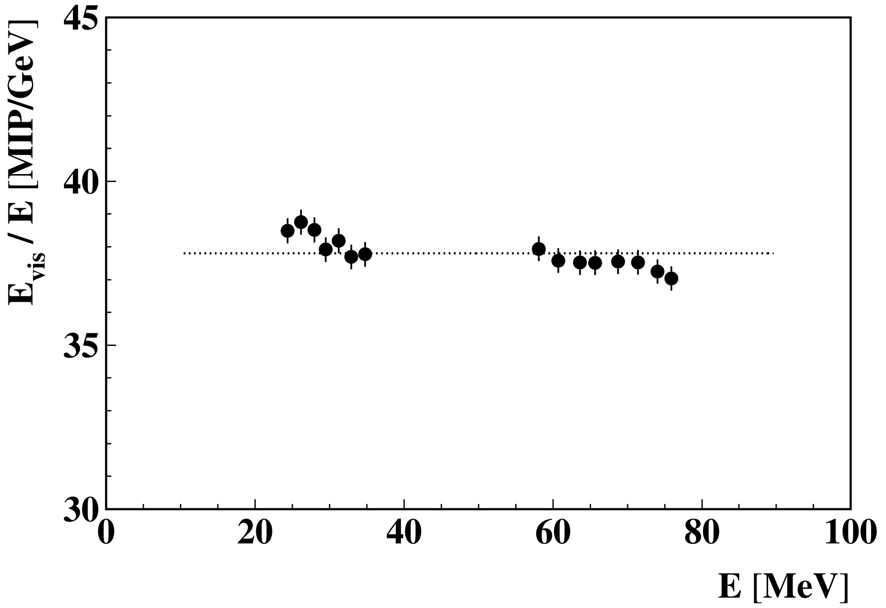

Fig. 6. Differential energy response for photons.

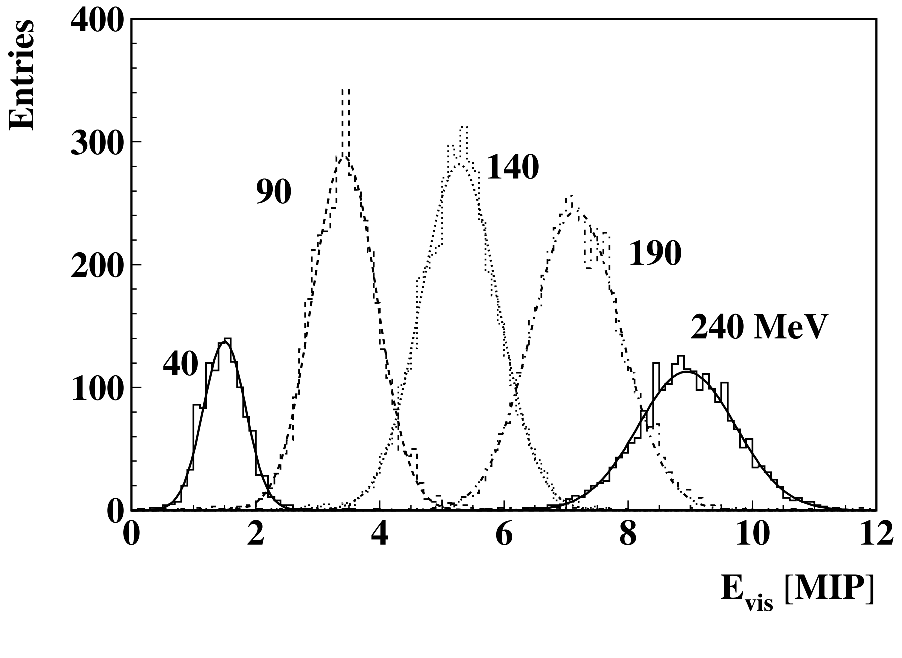

Fig. 7. Energy spectra for positrons.

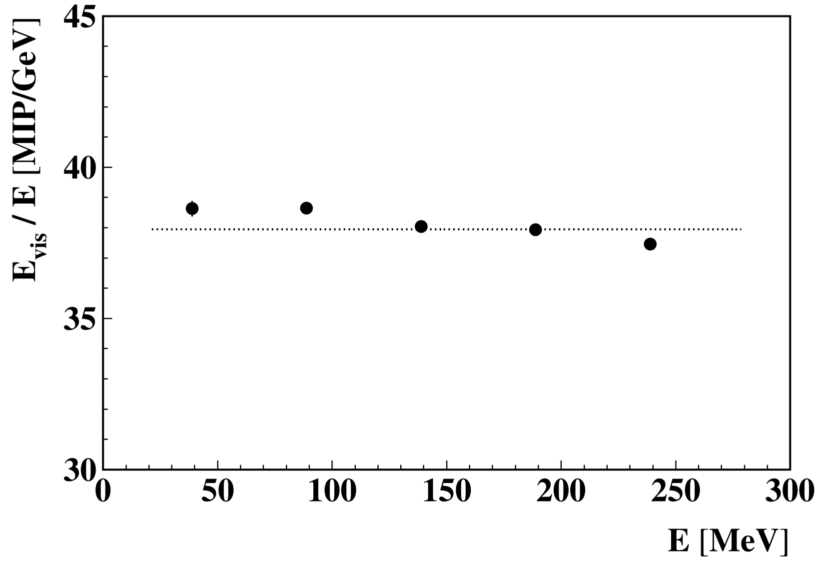

Fig. 8. Differential energy response for positrons.

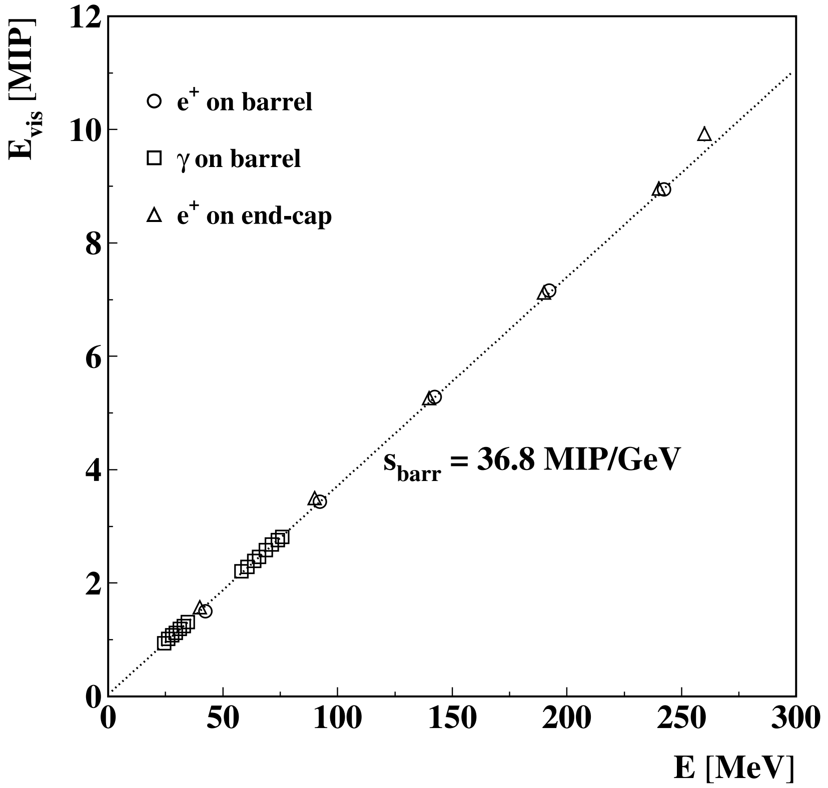

Fig. 9. Energy response for photons and positrons *vs.* kinetic energy.

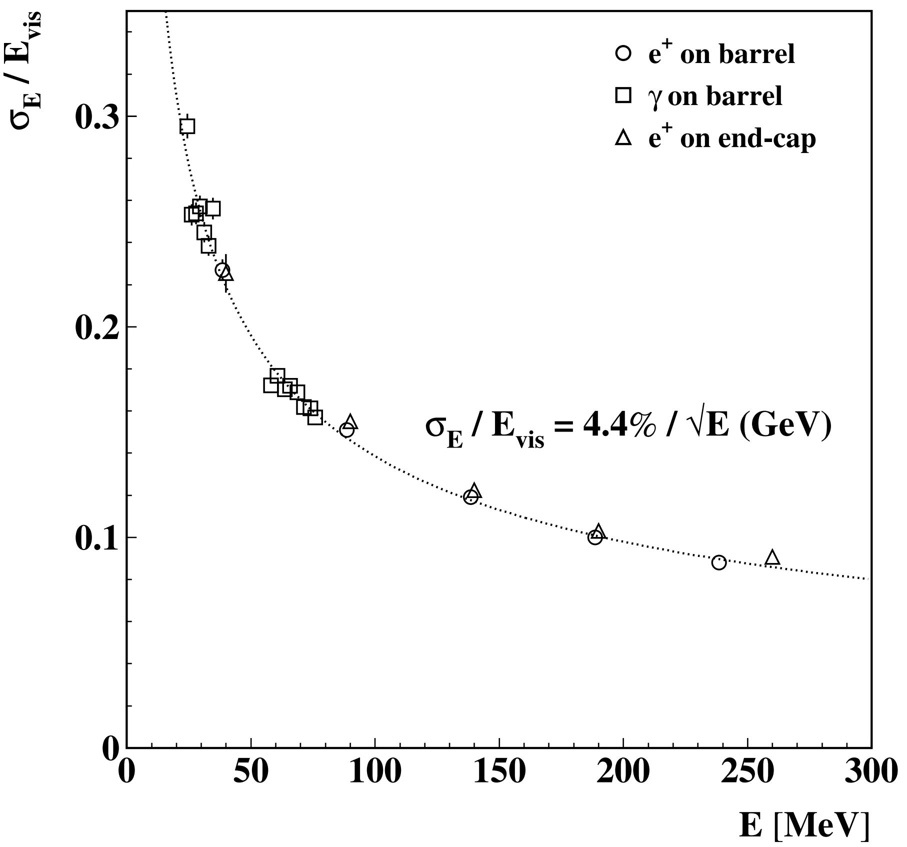

Fig. 10. Energy resolution for photons and positrons *vs.* kinetic energy.

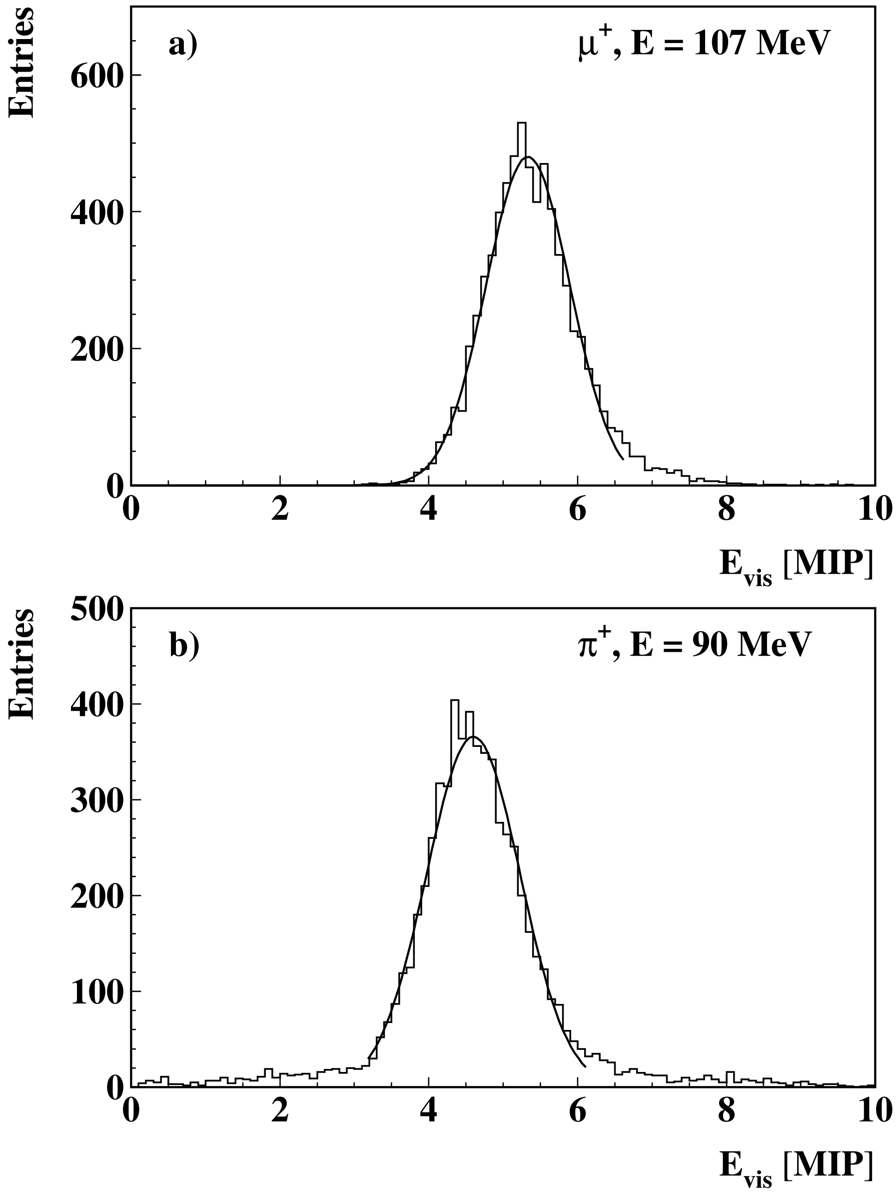

Fig. 11. Energy spectra a) 107 MeV muons and b) 90 MeV pions.

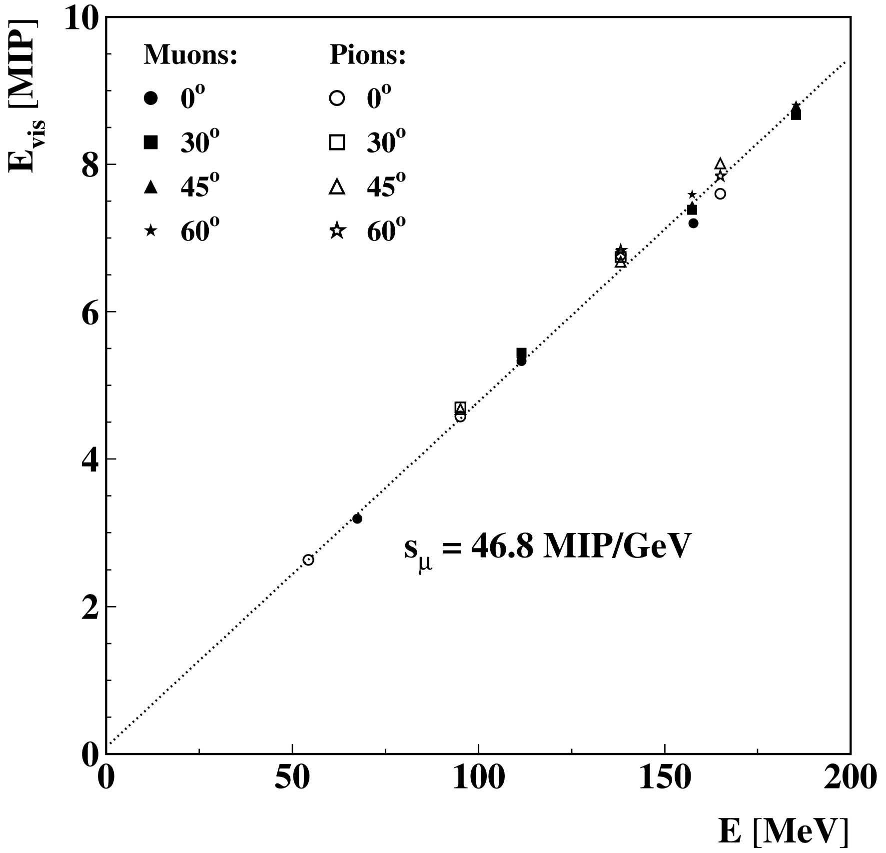

Fig. 12. Energy response for muons and pions *vs.* kinetic energy.

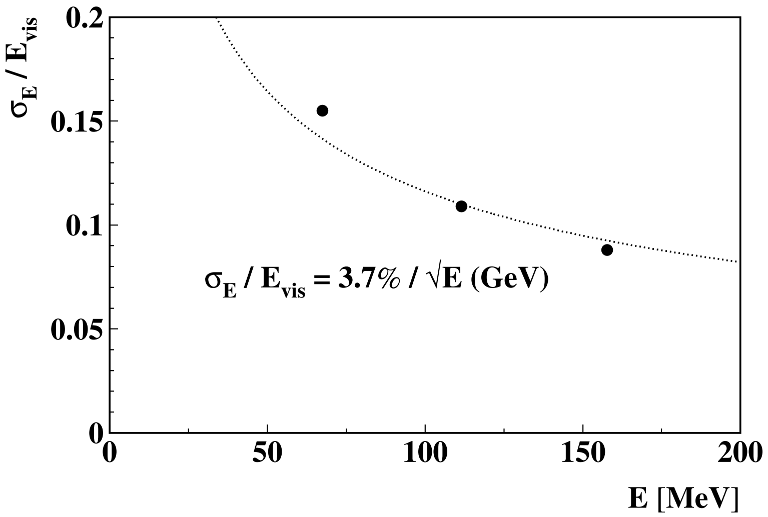

Fig. 13. Energy resolution for muons.

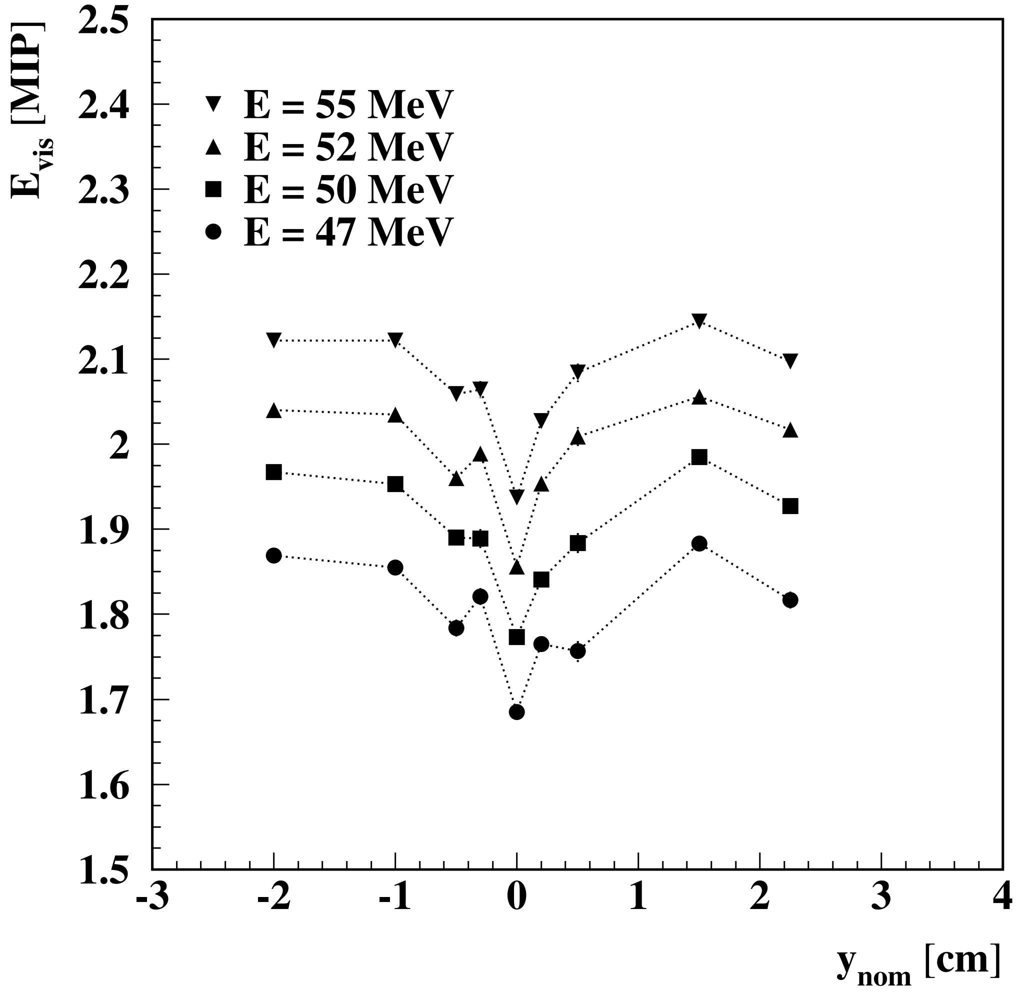

Fig. 14. Energy response *vs.* y–position.

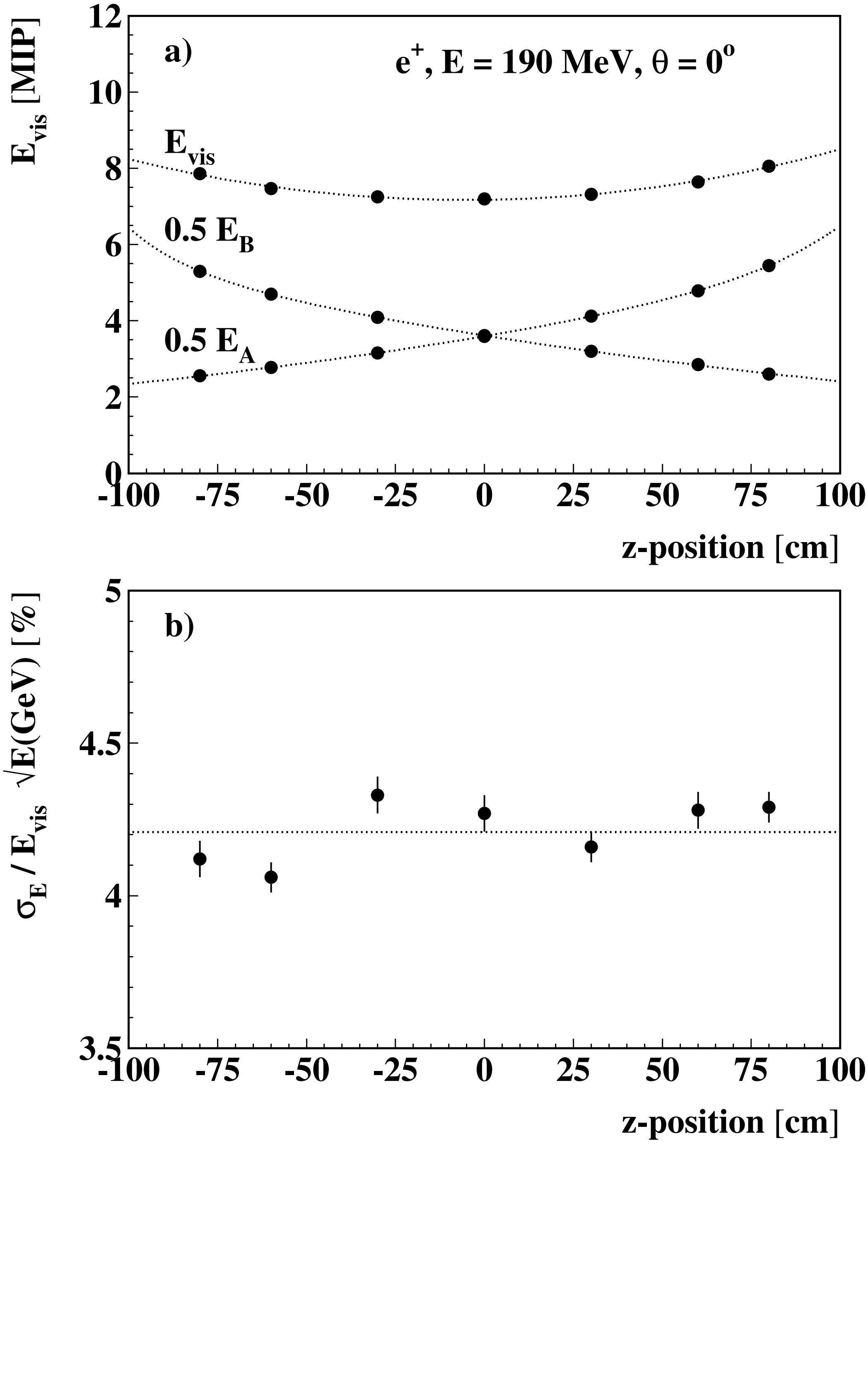

Fig. 15. a) Energy response *vs.* z–position, b) Energy resolution *vs.* z–position.

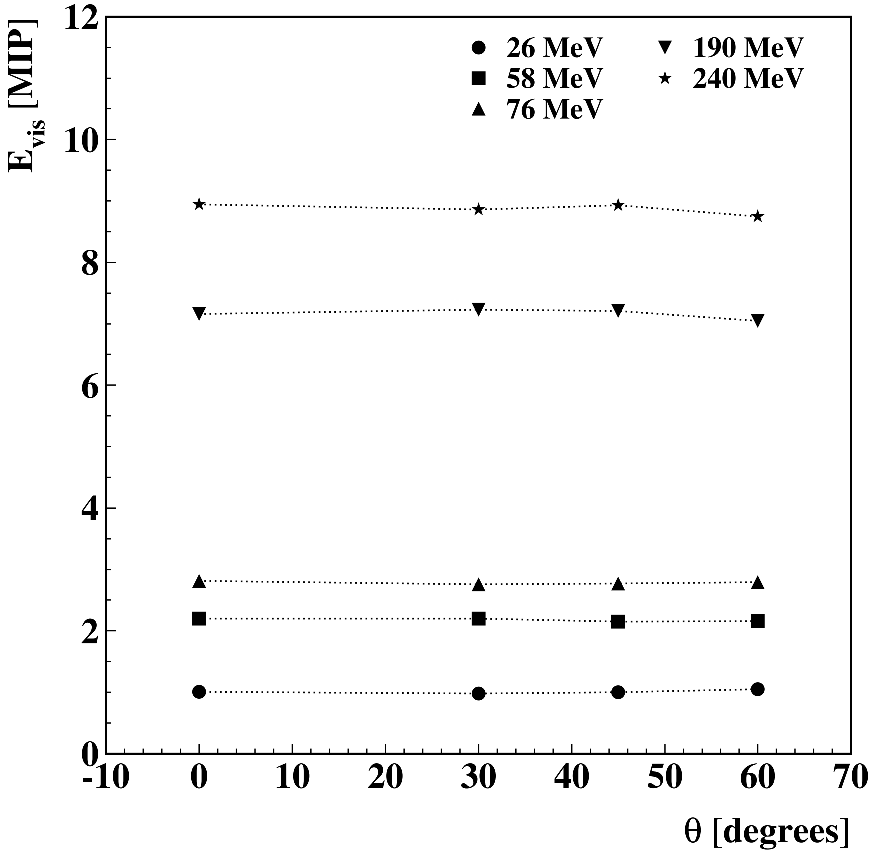

Fig. 16. Energy response *vs.* incidence angle θ.

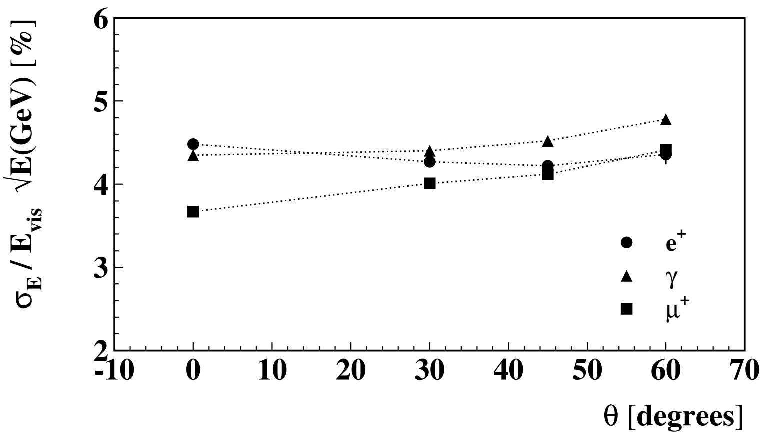

Fig. 17. Energy resolution *vs.* incidence angle θ.

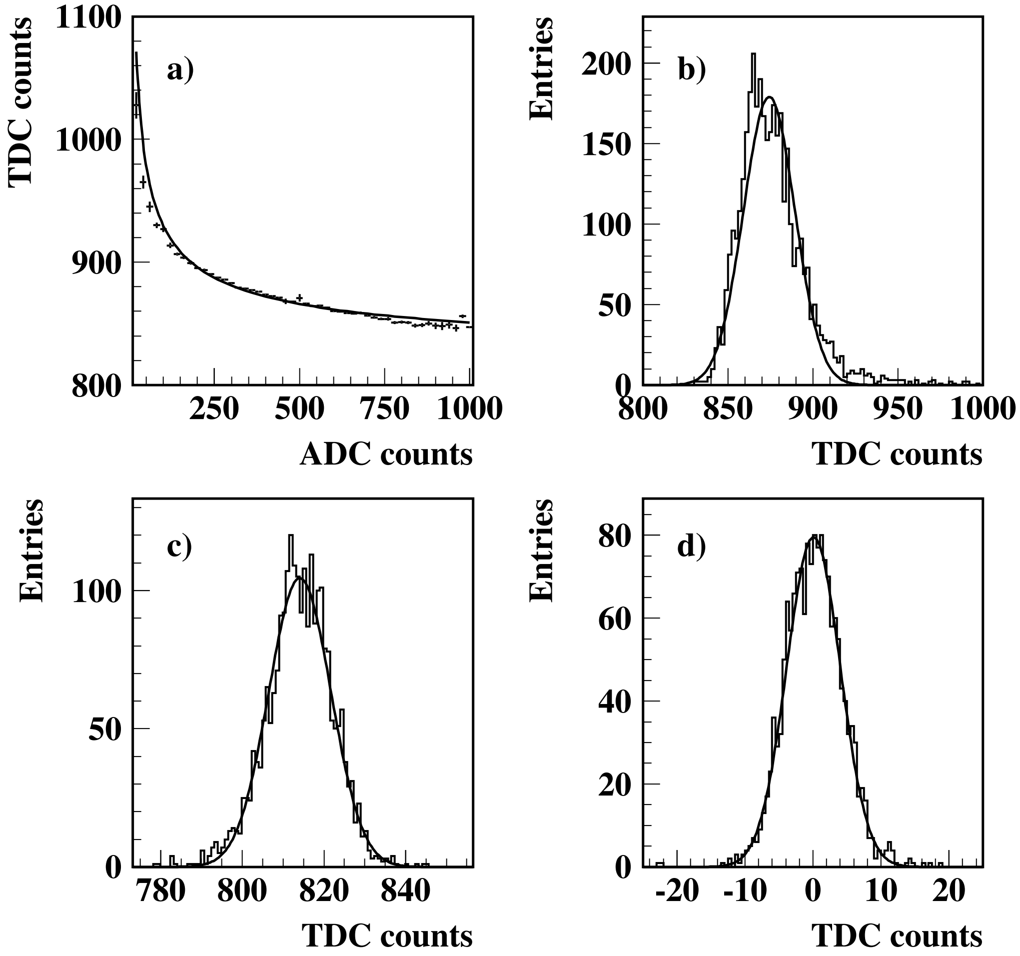

Fig. 18. a) TDC – ADC correlation,

b) time distribution for a single cell before correction,

c) the same distribution after walk correction,

d) time distribution summed over all cells.

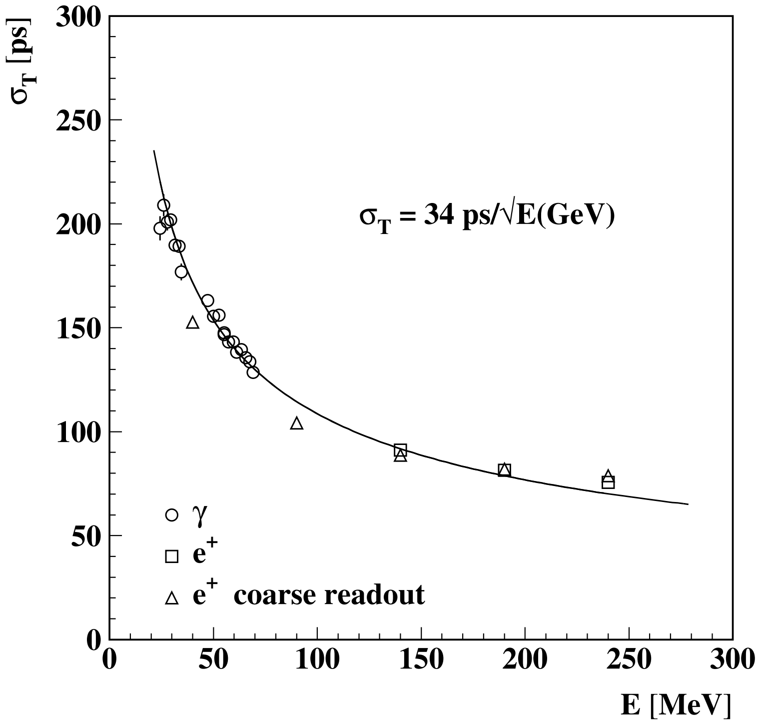

Fig. 19. Time resolution *vs.* energy.

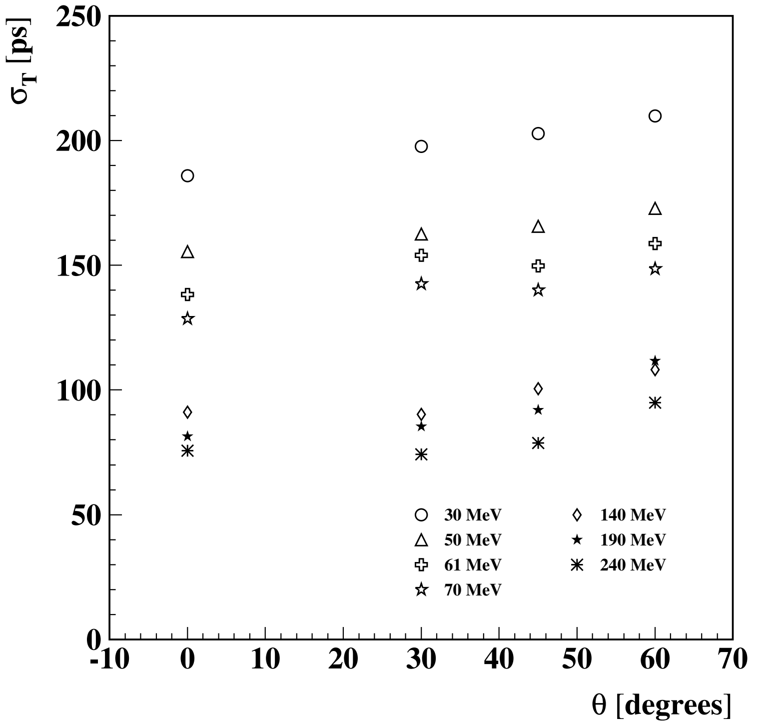

Fig. 20. Time resolution *vs.* incidence angle θ.

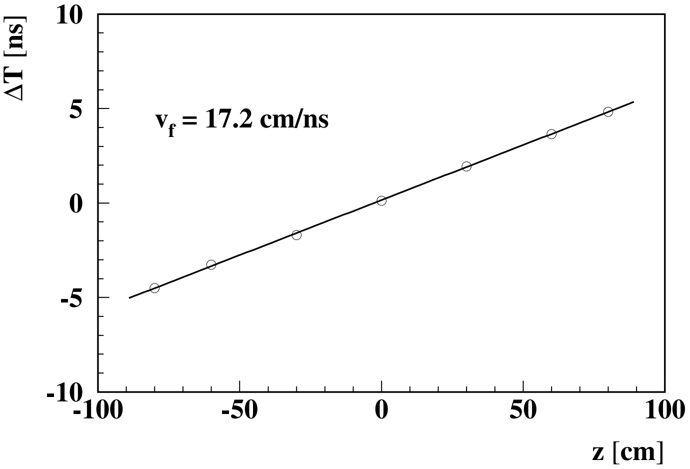

Fig. 21. ΔT distribution *vs.* nominal z-position for 190 MeV positrons.

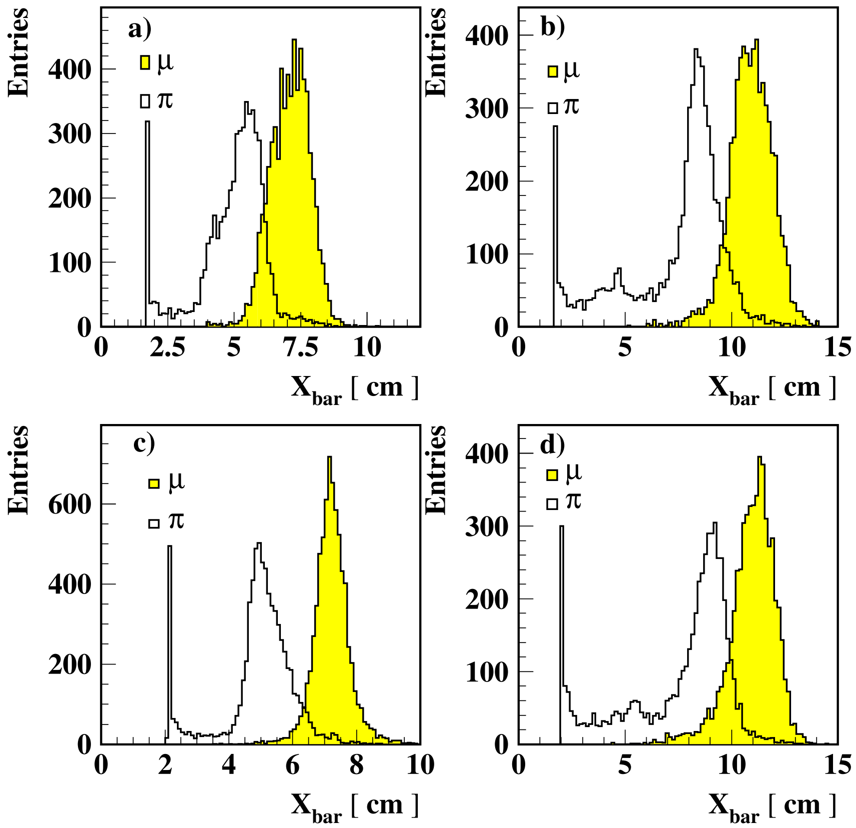

Fig. 22. X_{bar} distributions
for 3.5 cm granularity: a) 200 MeV/c, b) 250 MeV/c,
for 4.2 cm granularity: c) 200 MeV/c, d) 250 MeV/c.